AGU PUBLICATIONS

JGR

Journal of Geophysical Research: Solid Earth

RESEARCH ARTICLE
10.1002/2016JB013690

Key Points:
- A novel data-driven strategy for monitoring induced seismicity that combines generalized inversion and genetic algorithm is presented
- Studying the seismicity at The Geysers geothermal field, we found different dynamic rupture processes for smaller and larger earthquakes
- Two groups of events suggest the reactivation of deep structures and an important role of steeply dipping fault in fluid pressure diffusion

Supporting Information:
- Supporting Information S1

Correspondence to:
M. Picozzi,
matteo.picozzi@unina.it

Citation:
Picozzi, M., A. Oth, S. Parolai, D. Bindi, G. De Landro, and O. Amoroso (2017), Accurate estimation of seismic source parameters of induced seismicity by a combined approach of generalized inversion and genetic algorithm: Application to The Geysers geothermal area, California, *J. Geophys. Res. Solid Earth*, *122*, 3916–3933, doi:10.1002/2016JB013690.

Received 27 OCT 2016
Accepted 5 MAY 2017
Accepted article online 9 MAY 2017
Published online 29 MAY 2017

Accurate estimation of seismic source parameters of induced seismicity by a combined approach of generalized inversion and genetic algorithm: Application to The Geysers geothermal area, California

M. Picozzi[1], A. Oth[2], S. Parolai[3], D. Bindi[3], G. De Landro[1], and O. Amoroso[1]

[1]Department of Physics "E. Pancini", University of Naples Federico II, Naples, Italy, [2]European Center for Geodynamics and Seismology, Walferdange, Luxembourg, [3]Helmholtz Centre Potsdam, GFZ German Research Centre for Geosciences, Potsdam, Germany

Abstract The accurate determination of stress drop, seismic efficiency, and how source parameters scale with earthquake size is an important issue for seismic hazard assessment of induced seismicity. We propose an improved nonparametric, data-driven strategy suitable for monitoring induced seismicity, which combines the generalized inversion technique together with genetic algorithms. In the first step of the analysis the generalized inversion technique allows for an effective correction of waveforms for attenuation and site contributions. Then, the retrieved source spectra are inverted by a nonlinear sensitivity-driven inversion scheme that allows accurate estimation of source parameters. We therefore investigate the earthquake source characteristics of 633 induced earthquakes (M_w 2–3.8) recorded at The Geysers geothermal field (California) by a dense seismic network (i.e., 32 stations, more than 17.000 velocity records). We find a nonself-similar behavior, empirical source spectra that require an ω^γ source model with $\gamma > 2$ to be well fit and small radiation efficiency η_{SW}. All these findings suggest different dynamic rupture processes for smaller and larger earthquakes and that the proportion of high-frequency energy radiation and the amount of energy required to overcome the friction or for the creation of new fractures surface changes with earthquake size. Furthermore, we observe also two distinct families of events with peculiar source parameters that in one case suggests the reactivation of deep structures linked to the regional tectonics, while in the other supports the idea of an important role of steeply dipping faults in the fluid pressure diffusion.

1. Introduction

Geothermal fields and faults are some of the manifestations and key interacting elements of a unique complex system within the crust. The complexity of such systems originates from the strong spatial heterogeneity of the medium properties and the time variable changes related to the periodic occurrence of deformation and fracture phenomena caused by the hydrothermal fluid circulation in their shallow part. Within such a system, besides natural tectonic seismicity, human underground operations such as fluid withdrawal or injection, drilling, hydro-fracturing, and reservoir impoundments can positively or negatively impact effective local stress, pore pressure, fluid migration, and strain in the subsurface and hence be responsible for induced and triggered earthquakes. Indeed, in geologically active areas such as geothermal zones, it is very likely that the crustal and cover rocks are in a critically stressed state and preexisting faults in quasi-critically stable state. In these conditions, anthropogenically generated perturbations during industrial operations can be sufficient to move the stress state of these preexisting faults from quasi-critically stable to unstable by increasing pore pressure at fault zones and triggered earthquakes be generated. In this case, the additional perturbing stress is often very small in comparison with the preexisting stress system but sufficient to advance the clock of an event that would have eventually occurred anyway although probably at a later time [also, e.g., *Zoback*, 2012; *Ellsworth*, 2013].

The risk of generating triggered earthquakes is dramatically increased by industrial operations having the goal to artificially increase the permeability of subsurface hot rock masses and produce geothermal energy economically on a commercial scale. The operations of hydraulic fracturing, high-rate water injection, and/or chemical stimulation carried out to improve and potentially expand the heat extraction operations that started to be developed in the early 1970s in the USA lead to the definition of Enhanced Geothermal System (EGS). The main concept of this technology is simple: introduce fluids into a volume of thermally active lithology via fracture stimulation, then extract the hot fluids to produce thermal and electrical

energy, with the typical target range for electricity generation being between 3 and 6 km. Nowadays, many EGS projects are operative or under development (e.g., Rosemanowes, Hijiori, Ogachi, Soultz, Coso, Desert Peak, Glass Mountain, The Geysers, and Clear Lake). In the near future, similar fields may be developed in other regions, such as in Southern Tuscany or in similar geological context to the Molasse Basin (Switzerland, Germany, and Austria) such as the Padana Plain in Northern Italy.

In the past, EGS did not produce events large enough to disturb the local population; however, more recently projects attempting to develop systems in the shallow crust (i.e., 4.5–5.0 km of depth) at Soultz, Cooper Basin (Australia), and Basel (Switzerland) produced events approaching or exceeding magnitude 3. In particular, the 2006 M_L 3.4 event generated at Basel caused some considerable public alarm with associated very large total insurance claims [*Giardini*, 2009]. Despite the immediate shut-off of the injection activities, three events with magnitudes exceeding M_L 3.0 occurred 1–2 months after bleed-off [*Deichmann and Giardini*, 2009] and minor, sporadic microseismic activity is still occurring years later.

The Basel EGS example shows that continuous, real-time seismic monitoring of the time and space variation of induced seismicity is required not only to control and optimize the production [e.g., *Eberhart-Phillips and Oppenheimer*, 1984; *Stark*, 2003] but also for mitigating the seismic risk associated to triggered earthquakes. It becomes therefore very important to be able to obtain rapid and accurate determination of stress drop, dynamic stress release, and seismic efficiency, which together with high accurate location can provide insights into the dynamics of the earthquake rupture. Spectral parameters of microearthquakes can be estimated by both parametric [e.g., among others *Shearer et al.*, 2006; *Kawase*, 2006; *Tsuda et al.*, 2010; *Goertz-Allmann et al.*, 2011; *Kwiatek et al.*, 2011, 2014; *Zollo et al.*, 2014; *Ross and Ben-Zion*, 2016] and nonparametric [e.g., among others *Castro et al.*, 1990; *Parolai et al.*, 2004; *Oth et al.*, 2008, 2009, 2010] approaches.

Here we propose an improved nonparametric, data-driven strategy suitable for microseismic monitoring applications, which combines the generalized inversion technique with a genetic algorithm optimization approach. This technique allows at the first stage the extraction from the seismic recordings of empirical functions describing the seismic source, the site response, and the attenuation. In the second stage, the source spectra are inverted by a nonlinear optimization method, based on genetic algorithms, with the capability of simultaneously exploring the parameter space locally and globally for optimal solutions in terms of source parameters. Concerning this last step of the analysis, this study proposes a novel strategy, which consists in including the sensitivity of the source spectra to the source parameters into the inversion process. This strategy enhances the capability of genetic algorithms to converge toward the optimal solution and therefore allows to obtain an accurate characterization of the seismicity.

The procedure has been applied on the data set collected at The Geysers (hereinafter TG) geothermal field in California, one of the most productive geothermal field in the world [e.g., among others *Majer and Peterson*, 2007; *Bertani*, 2012] and a unique site for testing procedures, given the large amount of seismic data collected since 2007 by a dense surface seismic network operated by the Lawrence Berkeley National Laboratory Geysers/Calpine (http://www.geysers.com/seismicity.aspx).

In the following, we first shortly introduce TG area, network, and data set. Then, we describe the two-step inversion procedure, which we applied to about 600 events with magnitude $\geq$2 recorded from October 2009 to June 2011. Finally, the outcomes of our analysis are discussed in relation with findings and interpretative models of the geothermal field obtained by previous studies realized in the same area.

2. TG Area, Data Set, and Preprocessing

TG is a vapor-dominated geothermal reservoir in operation since the 1960s. The reservoir is hosted within the fractured Franciscan metagraywacke above a Pleistocene felsite intrusion [*Hartline et al.*, 2015]. Generally, the reservoir is considered made up of two main parts as function of the different temperature at depth: the first portion (i.e., normal reservoir or low-temperature zone (LTZ)) of the reservoir is spread below the whole geothermal field at a depth between ~2.75 km and a temperature of ~240°C; the second portion (high-temperature zone (HTZ)) extends from ~2.75 to ~4 km depth with temperatures of ~340°C [*Stark*, 2003; *Beall et al.*, 2010; *Jeanne et al.*, 2014a]. The geothermal area can also be considered divided into two distinct seismicity source zones along the northwestern to southeastern direction, hereinafter named Zone

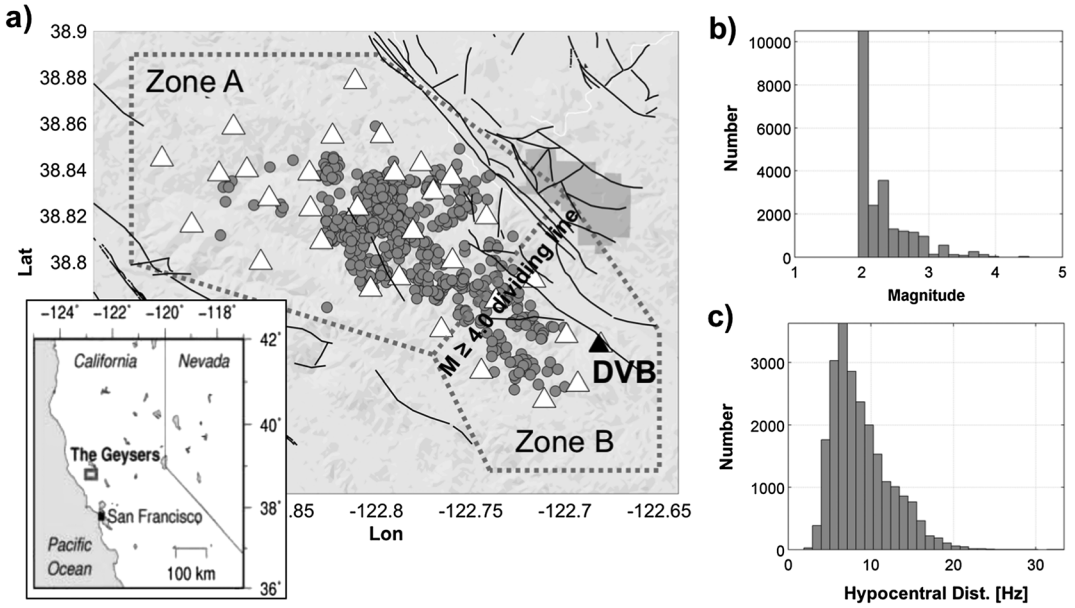

Figure 1. (a) Map of The Geysers area with relocated earthquakes (gray circles), seismic stations of the Lawrence Berkeley National Laboratory Geysers/Calpine seismic network (white triangles and black triangle for the reference station DVB), and quaternary fault structures (black lines). The gray dashed lines outline the seismic source Zone A and Zone B. (b) Distribution of records in terms of magnitude. (c) Distribution of records in terms of hypocentral distance.

A and Zone B, respectively (Figure 1a). The two zones were proposed by *Stark* [2003] after having observed differences in the seismicity distribution, with the southeastern part seismically less active than the northwestern one. The latter also presents seismicity at greater depth, which in turn is related to the depth variation in the high-temperature vapor-dominated reservoir. *Beall and Wright* [2010] suggested an "$M \geq 4.0$ dividing line" with northeast to southwest trend between the two zones, after having observed that Zone B is characterized by lower magnitude events. *Convertito et al.* [2012] confirmed the different seismic behavior of the two zones studying the *b* values of the Gutenberg-Richter relationship. Exhaustive reviews of the TG geothermal area and of the EGS demonstration project have been presented by *Jeanne et al.* [2014a] and *Garcia et al.* [2016].

The data set considered in this study is made freely available by the Northern California Earthquake Data Center (NCEDC) and consists of 633 events (Figure 1) in the magnitude range between M_L 2 and M_L 4.5 (i.e., the NCEDC catalog reports mostly duration and local magnitudes, which we consider equivalent), hypocentral distances between 0.1 and 33 km, recorded from October 2009 to June 2011 by the 32 three-component stations of the Lawrence Berkeley National Laboratory Geysers/Calpine (BG) surface seismic network.

The BG stations are distributed in an area of about 20 × 10 km^2, covering the entire geothermal field (Figure 1). During the considered period, each station was equipped with an Oyo GS-11D 4.5 Hz sensor and the data were sampled at 500 Hz. For all the selected events, we manually picked the corresponding *P* and *S* wave first arrival times. The events had then been re-located by a nonlinear probabilistic earthquake location code (http://www.alomax.net/nlloc) in 3-D *P* and *S* wave velocity models optimized for the area, obtained by *Amoroso et al.* [2015] through a linearized tomographic approach [*Amoroso et al.*, 2014]. Traveltimes are calculated by numerical integration of the slowness along the ray traced in the finite difference traveltime field [*Latorre et al.*, 2004]. The events have a minimum location error of 0.3 km.

The waveform data set consists therefore of more than 17.000 velocity records. Preprocessing consisted in correcting for the instrumental response and removing the linear trend. The Fourier amplitude spectra (FAS) were computed on time windows starting 0.1 s before the *S* wave onset and, following *Abercrombie* [1995], having variable length depending on the magnitude: 1 s windows for events $M < 3$, 2 s windows for events $3 \leq M \leq 4$, and 4 s for larger events. All windows were padded to 8 s to get the same spectral resolution of 0.125 Hz. The FAS were multiplied by ω (where $\omega = 2\pi f$, with *f* as the frequency) to get spectra in

acceleration, which were smoothed by a filter with variable frequency band equal to 25% of the central frequency. Finally, the spectra of the horizontal components were combined into their root-mean-square average. For the following analyses, we selected the spectral amplitudes of 50 frequencies equally spaced on a logarithmic scale over the range of 2–50 Hz. Preevent noise windows of the same length as signal were used to compute the signal-to-noise ratio (SNR). A minimum SNR of 10 is imposed at any FAS used in the inversion.

3. Generalized Inversion Technique

The *S* wave FAS is considered in log domain being the linear combination of the source spectra, *S*; the attenuation, *A*; and site response *Z*, which can be written as

$$\log_{10} U_{ij}(f, M_i, r_{ij}) = \log_{10} S_i(f, M_i) + log_{10} A(f, r_{ij}) + \log_{10} Z_j(f), \quad (1)$$

where the symbols *i* and *j* indicate the *i*th earthquake and the *j*th station, respectively; *M* is the magnitude; *f* is the frequency; and r_{ij} is the hypocentral distance.

The isolation from the *S* wave FAS of the *S*, *A*, and *Z* contributions can be performed by parametric approaches [e.g., among others *Kawase*, 2006; *Tsuda et al.*, 2010; *Zollo et al.*, 2014], where the unknown functions relating the source and propagation are expressed by standard models. On the opposite side, nonparametric inversion scheme [e.g., among others *Castro et al.*, 1990; *Parolai et al.*, 2004; *Oth et al.*, 2008, 2009, 2010; *Ameri et al.*, 2011] are data-driven strategies capable of extracting empirical functions of *S*, *A*, and *G*.

In this work, we have used the processing procedure proposed by *Oth et al.* [2011], which consists of one-step nonparametric generalized inversion technique (GIT). The adopted algorithm is a variant of the original approach proposed by *Castro et al.* [1990], which resulted to be particularly suitable for large data sets characterized by high numbers of recordings per stations and each event recorded at several stations. For each frequency, the inversion has been performed in a least squares sense [*Paige and Saunders*, 1982] and 200 bootstrap replications have been considered to assess the uncertainties [*Efron*, 1979]. After some tuning, the hypocentral distance range from 2 to 33 km has been discretized into 62 bins, each 0.5 km wide. The distances are computed along the rays traced in 3-D *P* and *S* wave velocity fields.

One of the main advantages of the GIT method is that it does not require any a priori assumption on the functional form of the attenuation operator, which allows to avoid assumptions on *Q* or geometrical spreading, and eventually to capture trends of the attenuation related with distance, for instance, the effect of lateral arrivals. However, it is worth noting that the unresolved degree of freedom affecting equation (1) must be removed by adding some constraint. The constraints adopted in this work are the following: (a) the attenuation operator is set to 1 at a reference distance, r_0, for any frequency (for which we have used 5 km, also aiming to avoid eventual near-field effects on the source spectra), (b) the attenuation varies smoothly with distance, and finally, (c) a reference condition must be set to eliminate the linear dependence between source and site (i.e., the site amplification is set to one for one or more reference stations). Similar to *Pacor et al.* [2016], we have selected one station (i.e., DVB) to act as site effects free reference, after checking the horizontal-to-vertical (*H*/*V*) spectral ratios (i.e., *H*/*V* with small-amplitude peak, <2.5; Figure S1 in the supporting information). We refer the readers to *Castro et al.* [1990] for details on the implementation of these constraints.

A detailed discussion of the attenuation and site characteristics in TG area is not the primary target of this work, and thus, these aspects will be examined in-depth in future studies together with results of tomographic analysis. Information on the empirical attenuation and results of preliminary analyses performed to isolate the contribution due to geometrical spreading from anelastic attenuation are presented in Figure S1. Similarly, the GIT and H/V site response estimates are shown in Figure S2.

4. Source Spectra Inversion

4.1. Source Model

The second part of the study focuses on the source spectra *S*(*f*) obtained from the GIT aiming at deriving the source parameters (i.e., seismic moment, M_o; corner frequency, f_c; and the parameter γ controlling the high-

frequency spectral falloff). For the inversion analysis, we have assumed an ω^{γ} source model, where the displacement source spectra have the form

$$S(f) = \frac{R^{\theta\varphi} VF}{4\pi\rho v_S^3 R_0} M(f), \quad \text{with} \quad M(f) = \frac{M_0}{1 + \left(\frac{f}{f_c}\right)^{\gamma}}. \tag{2}$$

The term $R^{\theta\varphi}$ represents the S wave average radiation pattern, which is set to 0.55 [*Boore and Boatwrigth*, 1984], the reference distance R_0 is set to 5 km according to the GIT analysis, the free surface factor F is 2, the separations of S wave energy onto two horizontal components is accounted by $V = 1/\sqrt{2}$, while v_S and ρ are the S wave velocity and density in the source region. Concerning these latter, we have used for each event the v_S value at the hypocenter location extracted from the tomographic velocity model proposed by *Amoroso et al.* [2015], while the density has been assumed equal ρ = 2.7 g/cm^3.

Source spectral fits have been carried out using a genetic algorithm [*Yamanaka and Ishida*, 1996], as described in the following section. Following the inversion analysis, stress drop ($\Delta\sigma$) estimates are computed following *Hanks and Thatcher* [1972]:

$$\Delta\sigma = \frac{7}{16} M_0 \left(\frac{f_c}{v_S}\right)^3, \tag{3}$$

while the radiated energy E_R is calculated from the inverted S wave spectra as proposed by *Izutani and Kanamori* [2001]:

$$E_R = \frac{4\pi}{5\rho v_S^5} \int_0^{\infty} |fM(f)|^2 df. \tag{4}$$

According to *Savage and Wood* [1971] and *Wyss* [1979], the seismic radiation efficiency, given by the ratio between radiated and total energy produced by the dislocation source, can be defined as the ratio of apparent stress (τ_a) and the averaged spatial stress ($\bar{\tau}$). However, as $\hat{\tau}$ is not directly measurable from seismic data, it is a common practice, following *Beeler et al.* [2003], to instead compute the Savage-Wood seismic efficiency η_{SW}, proportional by a factor 0.5 to the radiation efficiency and defined as

$$\eta_{SW} = \frac{\tau_a}{\Delta\sigma} = \mu \frac{E_R}{M_o \Delta\sigma}, \tag{5}$$

where the crustal shear modulus μ is set to $3.3 \cdot 10^{10}$ Pa.

The parameter η_{SW} allows to account for the stress overshoot, that is to discriminate between events for which the static stress drop is larger ($\eta_{SW} < 0.5$) or smaller (η_{SW} from 0.5 to 1) than the dynamic stress drop, computed as the initial stress minus the displacement-averaged shear strength spatially averaged over the seismic rupture (i.e., $\tau_0 - \hat{\tau}_k$ [see *Beeler et al.*, 2003]).

4.2. Sensitivity Analysis

A sensitivity analysis has been carried out to investigate which frequencies of the source spectra are most relevant for constraining each of the inverted parameters. According to *Arai and Tokimatsu* [2004], the sensitivity is computed as the absolute value of the nondimensional partial derivative of the source spectra, $\log_{10}(S_{(f)})$ with respect to the inverted parameters P (i.e., M_o, f_c, and γ), and expressed as

$$D_j^P(f) = \left| \frac{P}{\log_{10} S(f_i)} \frac{\partial \log_{10} S(f_i)}{\partial P} \right|_{P=P_j}. \tag{6}$$

Hence, the larger is the value of D_j^P, the more sensitive a given portion of the source spectra is to variations of a parameter P_j.

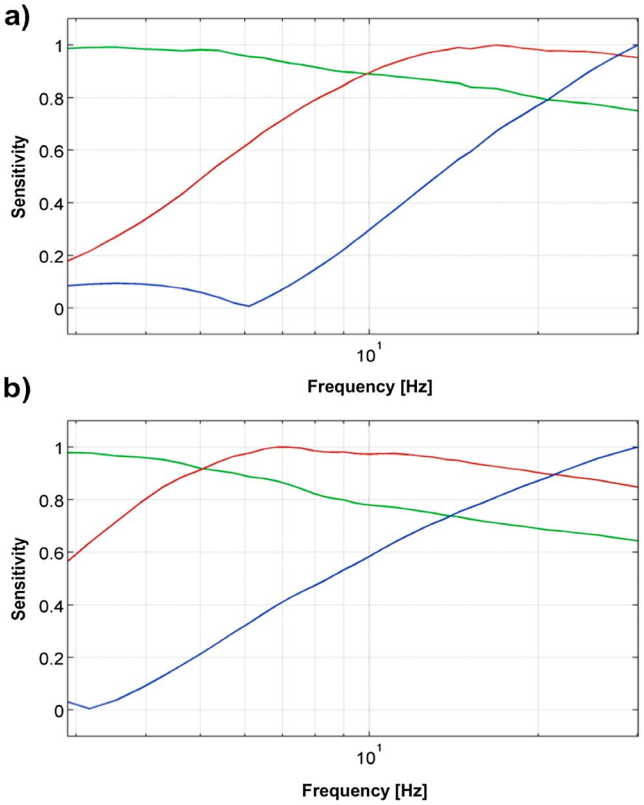

Figure 2. (a) Example of normalized sensitivity as a function of frequency for the parameters M_o (green), f_c (red), and γ (blue) for an event with magnitude M_w 2.4. (b) The same as Figure 2a but for an event with magnitude M_w 3.2.

The partial derivatives of $\log_{10}(S_{(f)})$ with respect to the parameters for each frequency i are

$$\frac{\partial \log_{10} S(f_i)}{\partial M_o} = 1, \quad (7)$$

$$\frac{\partial \log_{10} S(f_i)}{\partial f_c} = \frac{\gamma \cdot {f_i}^{\gamma}}{\ln(10) \cdot f_c \cdot \left(f_c^{\gamma} + f_i^{\gamma}\right)}, \quad (8)$$

$$\frac{\partial \log_{10} S(f_i)}{\partial \gamma} = \frac{-\ln\left(\frac{f_i}{f_c}\right) \cdot \left(\frac{f_i}{f_c}\right)^{\gamma}}{\ln(10) \cdot \left[1 + \left(\frac{f_i}{f_c}\right)^{\gamma}\right]}, \quad (9)$$

Figure 2 shows the variation of the normalized sensitivity, computed considering within equation (6) the observed source spectra, as a function of the frequencies with respect to the seismic source parameters M_o, f_c, and γ for two events having different magnitude (i.e., M_w 2.4 and 3.2). We observe that, as expected, the three source parameters are constrained by different portion of the source spectra, M_o, f_c, and γ being sensitive to the low-, medium-, and high-frequency parts of the source spectra, respectively.

4.3. Enhanced Genetic Algorithm

In this work, the estimation of seismic source parameters has been carried out using the genetic algorithm (hereinafter GA) proposed by *Yamanaka and Ishida* [1996]. GAs were originally proposed by *Keilis-Borok and Yanovskaya* [1967] and devised as a model of adaptation in artificial systems by using random numbers to control the characteristics of the search process [*Holland*, 1975]. With this algorithm, a search area for the parameters M_o, f_c, and γ is defined, and for each of them large search ranges were chosen. Concerning M_o, we defined the range to ±1 magnitude unit around the M_L from NCEDC bulletin, values which in turn were converted in M_o range limits using the relation of *Hanks and Kanamori* [1979]. Combining the minimum and maximum M_o together with the minimum and maximum $\Delta\sigma$ (i.e., 0.01 and 10 MPa), the range on f_c is derived. The $\Delta\sigma$ range was selected both considering the available information for the area under study [e.g., *Kwiatek et al.*, 2011, 2014; *Convertito et al.*, 2015] and the tuning of the inversion parameters with which the GA inversion was performed. Finally, for γ we explored the range from 1 to 5.

Starting from an initial population of 200 individuals randomly generated, genetic operations (i.e., crossover, mutation, dynamic mutation, and elite selection) are used to obtain a new population with the same size, which is reproduced based on a cost function of each individual. After a few tuning tests, the crossover probability has been set to 0.9, while the mutation probability has been set to 0.05 at the beginning of the inversion, but this value is dynamically varied during the iterations. An exhaustive description of the method and examples of its application can be found in *Yamanaka and Ishida* [1996], *Parolai et al.* [2005], and *Picozzi et al.* [2005]. The iterations are terminated at the 151th generation, because we have verified that it corresponds to (i) no further significant reduction of the misfit and (ii) it allows the GA to well sample the parameter space around the global minimum at the price of a computational time around 15 s for each inversion.

While exploitative algorithms such as GAs get less likely trapped in local minima than linearized approaches, they are less efficient to converge toward the global minimum. Attempts of combining GAs with linearized

approaches in multistep inversion strategies have already been proposed in the literature [e.g., *Picozzi and Albarello*, 2007].

In this work, we propose a novel strategy, to our knowledge, which aims at including within the GA the pieces of information used by linearized approaches to converge toward the optimal solution. Indeed, although a series of iterative linearized inversion techniques exists, the kernel of this family of methods when applied to nonlinear problems is the linearization, which generally consists in computing at each iteration the partial derivative for the data with respect to the parameters of the model itself (i.e., the matrix of these partial derivatives is known as *Jacobian matrix*). Since the *Jacobian matrix* is constructed from the partial derivatives of the source spectra $S(f)$ with respect to M_o, f_c, and γ, we decided to use the normalized sensitivities of each parameter $D^P(f)$ (i.e., equation (6)) as weighting functions for the GA inversion through the cost function:

$$\mathrm{cost}_{D(f)} = \left(\frac{1}{\sum_{j=1}^{N} D^{M_o}(f) + \sum_{j=1}^{N} D^{f_c}(f) + \sum_{j=1}^{N} D^{\gamma}(f)}\right)^{*} \left\{ \left[\sqrt{\sum_{j=1}^{N} \left(D^{M_o}(f) \cdot \frac{S_o(f) - S(f)}{S_o(f)}\right)^2 / N}\right] + \left[\sqrt{\sum_{j=1}^{N} \left(D^{f_c}(f) \cdot \frac{S_o(f) - S(f)}{S_o(f)}\right)^2 / N}\right] + \left[\sqrt{\sum_{j=1}^{N} \left(D^{\gamma}(f) \cdot \frac{S_o(f) - S(f)}{S_o(f)}\right)^2 / N}\right] \right\}, \quad (10)$$

where the subscript o indicates the observed data and N is the number of data points (i.e., frequencies) in the displacement spectra.

As concerns the comparison between the "classic" GA and the "enhanced GA" that includes the sensitivity information, the results of our tests (Figures S3 and S4) suggest that the new inversion scheme improves the GA capability of converging toward the hypervolume where the global minimum lies and to better explore its surroundings. Similar indications are also obtained from a test with synthetic data, where we show how the trade-off between f_c and γ is mitigated by the enhanced GA inversion approach (i.e., see Text S4 and Figure S5 in the supporting information).

Source spectra were inverted considering 44 different frequencies between 2 and 30 Hz, nearly equidistantly spaced on logarithmic scale within the analyzed frequency range. The minimum frequency is the same as for the GIT analysis and represents a limit under which we cannot go for instrumental reasons (i.e., below 2 Hz the signal is dominated by the instrumental noise, as shown also in the example of Figure S6). In contrast, the upper limit was defined after inversion tests and checks of the spectra. Indeed, we observed that beyond about 30 Hz, most of the spectra uncorrected for the attenuation and site effects for the same event present a change in the trend with increasing frequency (Figure S6). Such a trend is not introduced by the GIT-derived attenuation and site function corrections, being a feature visible already in the uncorrected data. At present, we cannot determine whether the origin of this feature is due to some hardware component, to the site installation, or to other unforeseen reasons, but certainly, it will be further investigated. As a result, including frequencies above 30 Hz could bias the optimization analysis, which is why we discarded them for the moment. In any case, we believe that in relation to the minimum magnitude of the data set at hand (i.e., M_w 2) and the low value of $\Delta\sigma$ observed for the area under study by other authors (i.e., ~ 2 MPa [*Convertito et al.*, 2015]), the maximum frequency of 30 Hz is well beyond the maximum expected corner frequencies (i.e., ~17.8 Hz), providing us with enough information to constrain both f_c and γ. This issue will be further considered during the discussion of results. A theoretical study on the reliability of estimates of source parameters of small earthquakes has recently presented by *Kwiatek and Ben-Zion* [2016]. Even per this latter study, given the sensor characteristics, the hypocentral distances, the magnitude range, and the level of seismic noise, reliable earthquake source parameters for The Geysers data can be estimated.

Figure 3 shows two examples of GA inversion results for events with magnitude M_w 2 and 3.5. During each inversion, more than 30000 models (Figures 3a and 3b, gray lines) were tested. For both events, the best fit model (green line) and those with misfit equal to the best fit plus 10%, 25%, 50%, and 100% (i.e., yellow, orange, red, and violet lines, respectively) fit the experimental source spectra equally well. This observation, together with the decreasing trend of the minimum misfit as function of the iteration number (i.e., number of generations; Figures S3 and S4) showing a rapid decrease during the first few tens of iterations and then a slower decrease, suggests the convergence toward the global minimum [*Yamanaka and Ishida*, 1996].

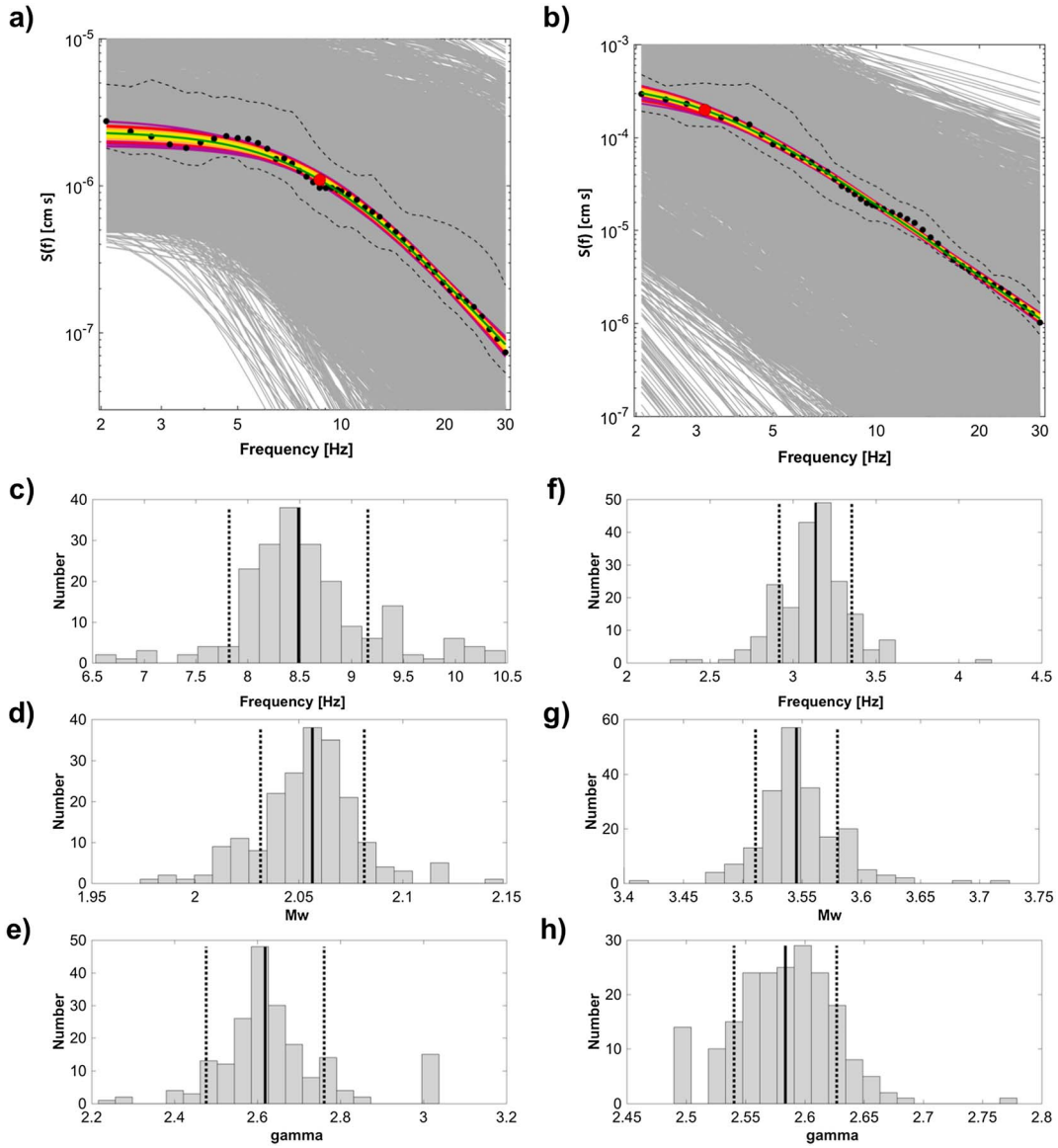

Figure 3. Results of the enhanced-GA inversion for an (left column) M_w 2 and (right column) M_w 3.5 events. (a) M_w 2 experimental source spectra (dots) ±1 standard deviation (dashed lines), tested models (light gray lines), minimum misfit model (green line), models lying inside the minimum misfit plus 10%, 25%, 50% and 100% (i.e., yellow, orange, red and violet lines, respectively), best fit model corner frequency (red dot). (b) The same as Figure 3a but for the M_w 3.5. (c and f) Distribution of f_c derived from the bootstrap analysis. Median value (black line) and ±1 standard deviation (black dashed lines). (d and g) The same as Figures 3c and 3f but for M_w. (e and h) The same as Figures 3c and 3f but for γ.

These results, in agreement to what was observed by *Parolai et al.* [2005] inverting surface wave curves with the same algorithm, indicate that despite the fact that the GA might not be able to single out the model that best reproduces the data set at hand, it still allows for a wide portion of the parameter space to be explored and the ensuing identification of the hypervolume where the global minimum lies [*Picozzi and Albarello*, 2007].

Figures S3 and S4 show the distribution of f_c, M_w, and γ for the models with misfit within the range of the minimum misfit plus the 10% together with the 16th and 84th percentiles (dashed black lines) and the mean value (black line). It is a common practice to provide estimates of the parameters uncertainty studying the variability of the inverted parameters related to models near the global optimal solution (e.g., models within some percentage of the minimum misfit value as shown in *Sonley and Abercrombie* [2006], *Viegas et al.* [2010],

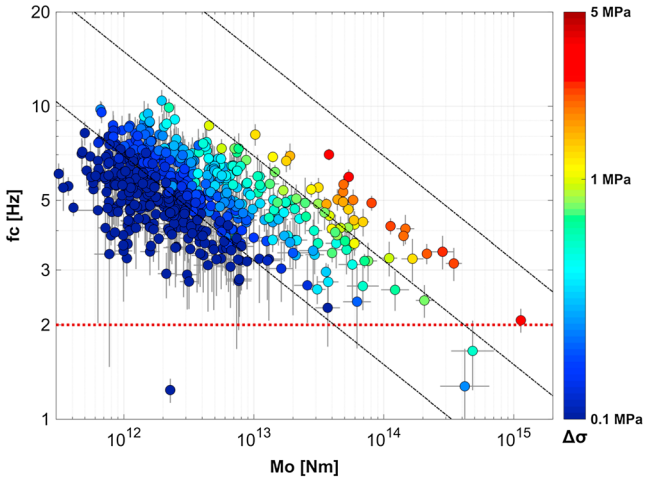

Figure 4. M_o and f_c (dots) colored per $\Delta\sigma$ values and standard error associated to the source parameters (horizontal and vertical black lines, respectively).

and *Abercrombie* [2013]). However, similar to what is done for the GIT analysis, in this work we performed 200 bootstrap replications for each inversion [*Efron*, 1979] and the parameters uncertainty has been assessed on the distribution of models with the best fit extracted at each replication (Figures 3c–3e and 3f–3h). During these analyses, to keep the total computational time as low as possible, we limited the generations to 51 for each inversion, after having verified that this configuration allows to find the best fit models. Figure 3 shows that in the case of well-fitted data the parameter distributions are narrow and the standard error is ~2% and ~7% of the value relevant to the best fit model for M_w, f_c, and γ, respectively.

5. Inversion Results

5.1. M_o, f_c, and $\Delta\sigma$

The enhanced GA inversion has been applied to the data set of 633 events at hand. For each inversion, we have selected the source parameter M_o, f_c, and γ of the best fit model, while the standard deviation of the parameters has been estimated from the bootstrap analysis. The misfit of the 633 best fit models plotted with respect to each inverted source parameters (Figures S7a–S7c) lead us to reject two source spectra poorly fitted. Therefore, we have selected 631 events of 633, which are considered well constrained and for which we study the source parameters. Figure S7d shows that the M_w estimates linearly correlate with the M_L from NCEDC with differences between the two characterized by null average and standard deviation of 0.18, and as discussed by *Deichmann* [2006] are likely to be ascribed to the way M_L is computed.

Figure 4 shows the seismic moments and corner frequencies for the analyzed data. Only for three events the corner frequency is estimated below 2 Hz, beyond the minimum frequency considered for the inverted spectra. Therefore, these events have been discarded. The standard error associated to the data is smaller for M_o than f_c, and for the latter is larger for small magnitude events. Even taking into consideration the uncertainty, we observe clear differences between smaller and larger magnitude events. For M_o smaller than about 10^{13} Nm (i.e., ~M_w 2.6) the data are rather scattered around low stress drop values (i.e., 1st, 50th, and 99th percentiles are equal to 0.013, 0.11, and 0.68 MPa, respectively). On the contrary, above 10^{13} Nm, despite a smaller number of events, we observe that $\Delta\sigma$ increases (i.e., 1st, 50th, and 99th percentiles equal to 0.12, 0.65, and 2.9 MPa, respectively).

In order to take the reservoir structure (i.e., temperatures exceeding 350 °C in the northwest sector at depth below ~2.75 km [*Jeanne et al.*, 2014a]) into consideration (at least at the first order), we split the source parameters in two subsets: (1) low-temperature zone (LTZ), with 418 events; and (2) high-temperature zone (HTZ), with 213 events.

The increase of $\Delta\sigma$ with M_w is at first glance a common feature for all events (Figure 5a), while the distribution of $\Delta\sigma$ with depth presents a peculiar feature (Figure 5b). Being related to the uncertainty on M_o and f_c, the uncertainty on $\Delta\sigma$ (i.e., the 95% confidence interval obtained propagating the uncertainty on M_o and f_c) is also larger for small magnitude events. Even considering the uncertainties for $\Delta\sigma$, the difference and trend of the data are, however, still clear. We observe that events with $M_w > 2.6$ belonging to both the LTZ (light gray circles) and HTZ (dark gray circles) do not show any clear trend, except for a small group of events (red circles) belonging to the HTZ that are characterized by $\Delta\sigma$ larger than 1 MPa (i.e., in total 23 events) and clustered in the depth range 2.9 km and 3.7 km (i.e., in agreement with the reservoir boundary given by the granitic

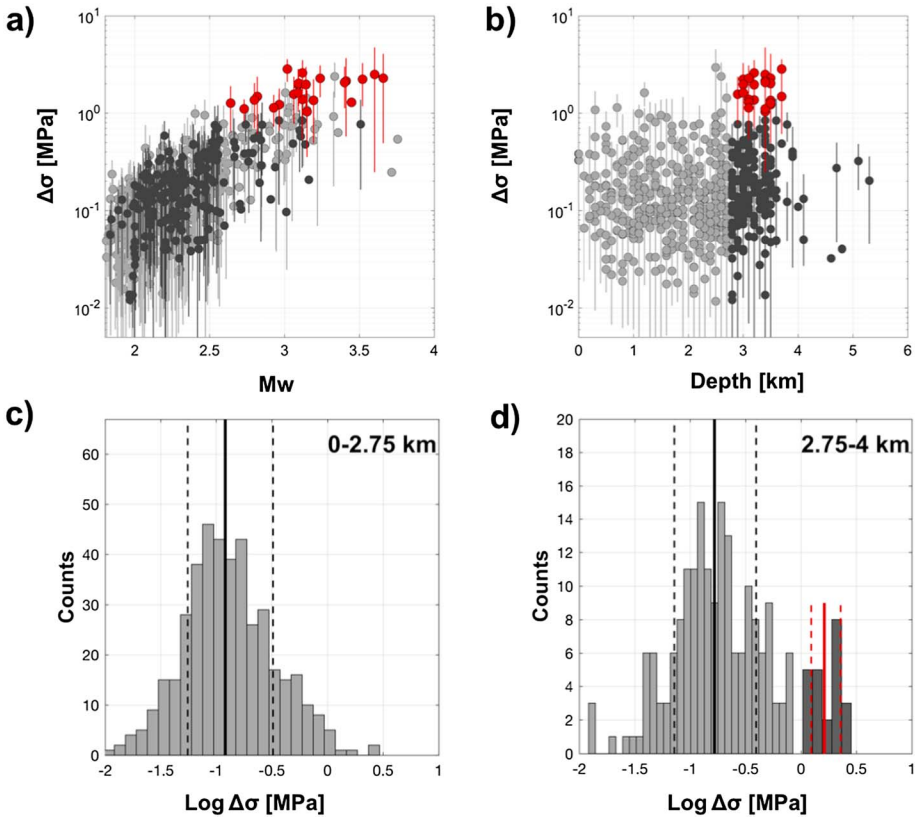

Figure 5. (a) $\Delta\sigma$ versus M_w for events within the LTZ (gray), within the HTZ (black), and within the HTZ but $\Delta\sigma \geq 1$ MPa (red). 95% confidence interval on $\Delta\sigma$ colored per the considered subset. (b) Similar to Figure 5a but $\Delta\sigma$ versus event depth. (c) Distribution of $\log_{10}(\Delta\sigma)$ for the depth range 0–2.75 km, with 16th and 84th percentiles (dashed black lines) and the mean value (black line). (d) The same as Figure 5c but for the depth range 2.75–4 km. Events with $\Delta\sigma < 1$ MPa (gray bars), with 16th and 84th percentiles (dashed lines) and the mean value (black line). Events with $\Delta\sigma \geq 1$ MPa (dark gray bars), with 16th and 84th percentiles (dashed red lines) and the mean value (red line).

intrusion that has an approximate depth of 4 km). These observations are confirmed by the distributions of events for different depth ranges (i.e., median $\Delta\sigma$ ~ 0.12 MPa and 0.16 for the depth ranges 0–2.75 km and 2.75–4 km, respectively; Figures 5c and 5d; median equal to ~1.6 MPa for events with higher $\Delta\sigma$ in the depth range 2.75–4 km; Figure 5d).

5.2. Seismic Radiation Efficiency, η_{SW}

Figure 6a shows the distribution of the radiation efficiency η_{SW} with respect to the magnitude. In this case, the uncertainty (i.e., the 95% confidence interval) has been derived from the uncertainty on M_o, $\Delta\sigma$, and the radiated energy. For the latter the uncertainty has been assessed from bootstrap analysis. Most of the events show values of η_{SW} smaller than the 0.3 threshold suggested by *Beeler et al.* [2003], which in first approximation allows the discrimination of events having dynamic weakening more than that observed during lab-experiments (i.e., $\eta_{SW} > 0.3$). The 50th percentile of the η_{SW} distribution is 0.18, a value to which also the events with $\Delta\sigma > 1$ MPa identified within the HTZ converge very well, despite the fact that they show larger uncertainty. Next, we focus on the events having η_{SW} that overcome the 84th percentile of the distribution (i.e., η_{SW} = 0.24; 68 and 31 events in the LTZ and HTZ, respectively). Even if the threshold η_{SW} = 0.24 is smaller than the 0.3 suggested by *Beeler et al.* [2003], events with higher η_{SW} may be characterized by specific dynamic features or spatial distribution and from now on are therefore considered separately (i.e., within Figures 6 and 7, they are shown as light and dark blue circles for LHT and HTZ subsets, respectively).

Figures 6b and 6c show that these events with high η_{SW} are characterized by both low $\Delta\sigma$ and mostly magnitude smaller than M_w 2.5, which in turn causes a larger source radius r (computed according to

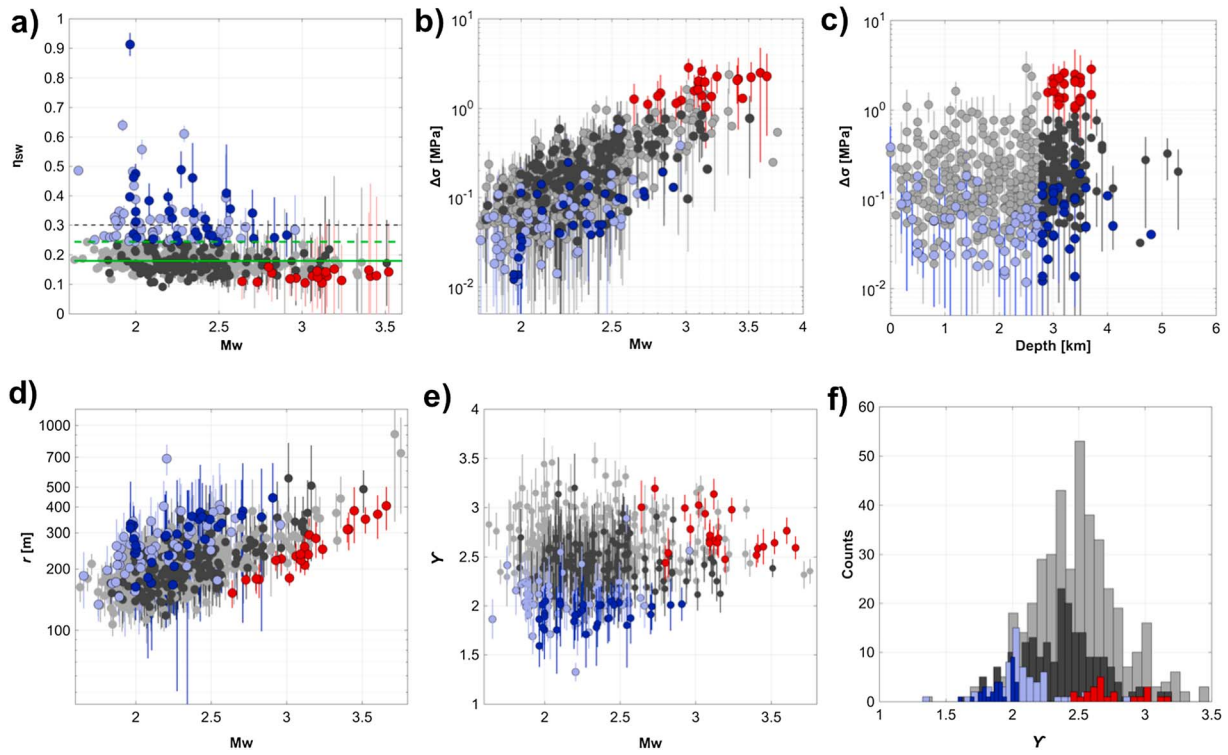

Figure 6. (a) Radiation efficiency η_{SW} versus M_w for events within the LTZ (gray), within the HTZ (black), and within the HTZ but $\Delta\sigma \geq 1$ MPa (red); threshold $\eta_{SW} > 0.3$ suggested by *Beeler et al.* [2003] (black dashed line), 50th (green line) and 84th (dashed green) percentiles of the η_{SW} distribution. Events having $\eta_{SW} > 0.24$ (84th percentile of η_{SW}) within the LTZ (light blue) and within the HTZ (dark blue). (b) $\Delta\sigma$ versus M_w. (c) Similar to Figure 6b but $\Delta\sigma$ versus event depth. (d) Similar to Figure 6b but r versus M_w. (e) Similar to Figure 6b but γ versus M_w. (f) Distribution of γ colored per subset according to Figure 6a.

Brune [1970]) than for the others. Figure 6d suggests an increase of r with magnitude for these events higher than that of all the others. On the opposite, the events having large $\Delta\sigma$ within the HTZ are characterized, for a given magnitude, by the smallest source radius dimensions. Figures 6e and 6f show that, as expected, the parameter γ and η_{SW} are inversely correlated, with all events with high η_{SW} presenting γ very close 2 (i.e., the ω^2 source model provides a good description of source spectral shapes only for these subset of events). On the contrary, all the other events, including those with high $\Delta\sigma$, show γ around 2.5 or higher.

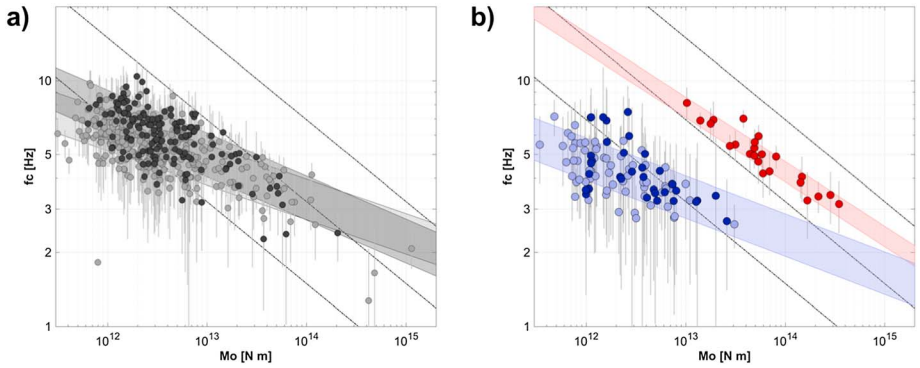

Figure 7. (a) M_o and f_c for two subsets of data: for events with $\Delta\sigma < 1$ MPa within the HTZ (dark gray dots), M_o versus f_c scaling relation ±1 standard deviation (dark gray area); for events with $\eta_{SW} < 0.23$ (light gray dots), M_o versus f_c scaling relation within the LTZ ±1 standard deviation (light gray area). (b) The same as Figure 7a but events with $\Delta\sigma \geq 1$ MPa within the HTZ (red dots); events with $\eta_{SW} > 0.23$ (light and dark blue dots for the LTZ and HTZ, respectively), M_o versus f_c scaling relation for events with $\Delta\sigma \geq 1$ MPa ±1 standard deviation (light red area), and for those events with $\eta_{SW} > 0.23$ ±1 standard deviation (light blue area).

5.3. Stress Drop Scale Dependence

Following *Oth* [2013], we have investigated the parameter ε, which, as suggested by *Kanamori and Rivera* [2004] allows to quantify how strongly $\Delta\sigma$ varies with M_o through the relation $M_0 \propto f_c^{-(3+\varepsilon)}$. Figure 6b already clearly indicates that earthquakes within the data set at hand are not self-similar (i.e., $\Delta\sigma$ increases with M_w).

In order to take the different trends observed in the source parameters into account, we estimate ε for four different subsets of data, i.e., (1) shallow events, removing those with high seismic radiation efficiency (i.e., $\eta_{SW} > 0.23$), (2) deep events removing those with high stress drop (i.e., $\Delta\sigma \geq 1$ MPa) and high seismic radiation efficiency, (3) deep events with high stress drop, and (4) shallow and deep events with high seismic radiation efficiency.

We find $\varepsilon = 4.4 \pm 0.48$ and $\varepsilon = 2.78 \pm 0.55$ for LTZ and HTZ events, respectively (i.e., subsets 1 and 2; Figure 7a), while $\varepsilon = 0.81 \pm 0.21$ for high $\Delta\sigma$ and $\varepsilon = 3.5 \pm 0.78$ for those with high η_{SW} (i.e., subsets 3 and 4; Figure 7b). Considering the errors associated to the parameters ε, the null hypothesis of self-similar scaling can be rejected at 95% confidence level for all the subsets of data. These results agree with the observation that source spectral shapes can be reproduced mostly with source models having a high-frequency spectral falloff γ larger than 2.

6. Discussion

The combination of a nonparametric approach allowing for the separation of the source spectra from the contribution of attenuation and site response with an innovative nonlinear inversion scheme applied on the retrieved empirical source spectra enables us to obtain accurate estimates of source parameters, and therefore a better characterization of the seismicity at TG geothermal field.

The outcome of our analysis provides compelling evidence that the seismicity at TG is characterized by low stress drop and high-frequency spectral falloff larger than 2 irrespective of depth (i.e., LTZ and HTZ).

Observing low $\Delta\sigma$ values for hydrofracture-induced earthquakes with respect to natural ones is not considered new evidence (e.g., among the others, see the review of *Abercrombie and Leary* [1993]). Low stress drop associated to induced seismicity is possibly related to the concomitant effects of different tectonic settings as compared with natural seismicity, such as shallower hypocentral depth and the injection of fluids, which may lower the effective stress causing the shear stress to overcome the Mohr-Coulomb failure criterion [*Goertz-Allmann and Wiemer*, 2012]. Besides these effects, the high temperatures characterizing both natural and EGS geothermal fields clearly play a significant role in the crustal mechanical behavior (e.g., the frictional strength), influencing the resulting seismicity. The thermal state of the crust has been found to influence also natural seismicity in Japan [*Oth*, 2013], where low stress drop values have been observed to be spatially related to high heat flow areas.

From the analysis of seismic data collected during geothermal operation in Basel, *Goertz-Allmann et al.* [2011] found an average $\Delta\sigma$ of 2.3 MPa and, most importantly, both a significant inverse relationship with respect to the distance from the injection point and an inverse correlation with estimates of the pore pressure. Similar observations of distance-dependence of $\Delta\sigma$ were also reported by *Kwiatek et al.* [2014] at the Berlìn Geothermal Field, El Salvador.

Concerning the TG geothermal field, *Kwiatek et al.* [2015] analyzed a spatially focused cluster of seismicity at the TG, located in the northwestern part of the geothermal field, in the proximity of the injection of the EGS wells Prati-9 and Prati-29. The refined analysis of 354 events with magnitude between M_w ~1 and M_w 3.2 by the spectral ratio method [*Kwiatek et al.*, 2011, 2014] highlights an average static stress drop of about 7 MPa assuming the Madariaga source model (i.e., ~1.7 MPa using the Brune Model). *Kwiatek et al.* [2015] found a clear relation of the seismic source characteristics to the injection flow rates and that prevalently shallower normal faulting events show smaller stress drop with respect to deeper strike-slip events. Somehow contrasting results concerning $\Delta\sigma$ were obtained by other authors in the same area, probably due to different assumptions on the source model, as well as on the attenuation and site corrections (e.g., *Viegas and Hutchings* [2011] found a median $\Delta\sigma$ of 28 MPa using the empirical Green's function technique and *Convertito et al.* [2015] reported $\Delta\sigma$ of ~2 MPa applying the iterative multistep spectral fitting approach proposed by *Zollo et al.* [2014]). Regarding this issue, we think that the data-driven GIT approach implemented in

this study allows for an effective correction of the attenuation and site contribution, and the nonlinear sensitivity-driven inversion scheme of the source spectra allows for an accurate estimation of $\Delta\sigma$ as well as the other source parameters.

The results concerning the high-frequency spectra falloff highlight interesting features of the TG seismicity. Indeed, $\gamma > 2$ as we have found would result in smaller radiated energy with respect to the typically applied *Brune* [1970] source model (i.e., $\gamma = 2$). According to the dynamic model proposed by *Madariaga* [1976], the observed relatively small high-frequency energy suggests that most of the TG seismicity is characterized by smooth rupture propagation. Moreover, following *Frankel* [1991], observing γ larger than 2 we can argue that the fault strength at the TG is not scale-invariant. The seismic radiation efficiency η_{SW}, related to the high γ, resulted for most of the events smaller than the 0.3 threshold suggested by *Beeler et al.* [2003], which indicates positive overshoot. These findings agree with the η_{SW} observed by *Zollo et al.* [2014] when analyzing the natural microseismicity in Southern Italy, a region where the crust is considered highly fractured and partially or completely saturated with fluids. Regarding the fluids at TG, both the original works of *Stark* [1992] and the recent studies of *Martínez-Garzón et al.* [2013, 2014] and *Jeanne et al.* [2014b] emphasize that their injection into the reservoir induces seismicity by both thermal and/or poroelastic stress changes.

Our results in terms of η_{SW} suggest that for most of the analyzed earthquakes the radiated energy is a small fraction of the energy spent for both the creation of new fracture surface and by friction (i.e., indicating high fracture efficiency and high dynamic strength of the medium). This result is in agreement with the experimental study of *Tenthorey and Cox* [2006] showing that hydrothermal reactions can play, depending on the rock rheology, temperature, and fluid composition, a significant role in helping the cement and compaction of faults.

The conceptual model of seismicity generation and fluid transport at TG proposed by *Kwiatek et al.* [2015] and derived studying earthquakes in the proximity of two EGS wells indicates that the injection of water at low temperatures (i.e., ~70 °C) induces seismicity mainly close to the wells by thermal stress, with seismic moment varying as a function of the thermal contrast between rocks and water, and clearly as function of depth (i.e., smaller M_o in the LTZ and higher Mo when water is injected directly within the HTZ). On the contrary, the seismicity at greater distances from the wells and at greater depths is mainly related to an increase of the pore fluid pressure. In particular, *Kwiatek et al.* [2015] found that the increase of poroelastic stress at larger depth is responsible for the changes in the kinematic properties of the events (i.e., from normal to strike-slip faulting mechanism dominance at smaller and greater depth, respectively), accompanied by an increase of stress drop.

An interpretation of the results of this study in terms of the conceptual model proposed by *Kwiatek et al.* [2015] is not straightforward, mainly because our data set does not include small magnitude events (i.e., M_w equal or smaller than 1) and the events are spread over the entire geothermal area, which makes it difficult to associate the variation of source parameters to the injection activity of specific wells. In this sense, our results provide a general overview of the TG seismicity characteristics, which may complement the spatially focused analysis of *Kwiatek et al.* [2015]. Despite the lack of a clear increase of $\Delta\sigma$ with depth for most of the earthquakes in our data set, we have interestingly found a distinct family of events that occurred within the HTZ of the reservoir and is characterized by higher $\Delta\sigma$. According to *Kwiatek et al.* [2015], these events, which range in magnitude between ~2.5 and ~3.5, might be related to the reactivation of deep structures linked to the regional tectonics. Supporting this hypothesis, Figure 8a shows that most of these higher $\Delta\sigma$ events are spatially distributed according to the general regional faults trend, characterized by right-lateral strike-slip faults.

The distribution of LTZ events, as well as of those characterized by $\gamma \sim 2$, relatively high η_{SW}, low $\Delta\sigma$, and magnitude mostly between ~2 and ~2.5 with hypocenters both within the LTZ and HTZ is shown in Figure 8b. The contour of the $\Delta\sigma$ values for these events shows a large area with low $\Delta\sigma$ in the northwestern sector and an almost north-to-south trending minimum in coincidence with the $M \geq 4.0$ dividing line separating Zones A and B.

A section drawn according to the regional faults trend (Figure 8c) shows that the high $\Delta\sigma$ events are distributed in two patches ~2 km wide between 3 and 4 km of depth, while the high η_{SW} events are spread over a wide range of depths (i.e., ~1 km and ~4 km) but interestingly appear quite well aligned vertically. We have identified three main alignments that have similar apparent dip (i.e., ~30°; Figure 8c), the first and third of which are approximately located in the middle of Zone A and B, respectively. The second alignment,

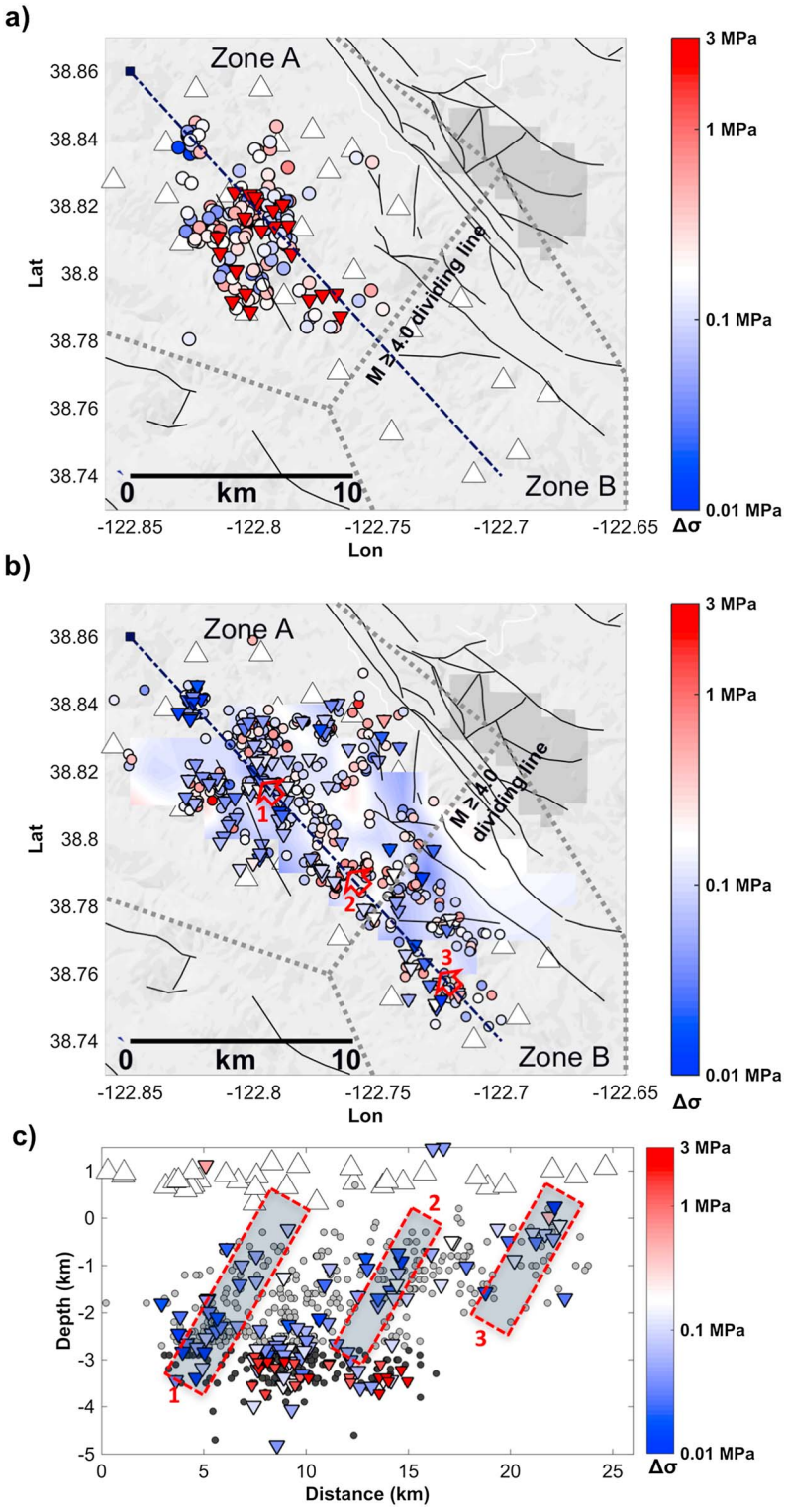

Figure 8. (a) Similar to Figure 1 but with events with $\Delta\sigma \geq 1$ MPa within the HTZ (red triangles) and those with $\Delta\sigma < 1$ MPa within the HTZ (dots colored per $\Delta\sigma$ values). The black dashed line roughly oriented NW-SE identifies the profile adopted for the depth section. (b) The same as Figure 8a but for events having $\eta_{SW} > 0.23$ (triangles) and those within the LTZ (dots) colored per $\Delta\sigma$ values. Contour of $\Delta\sigma$. The black dashed line roughly oriented NW-SE identifies the profile adopted for the depth section. (c) Depth section of the seismicity shown in Figures 8a and 8b. Alignments of $\eta_{SW} > 0.23$ events (light gray areas with red dashed boundary). Approximate projection on the surface of the three alignments of $\eta_{SW} > 0.23$ and events identified within Figure 8c (red arrows).

instead, is approximately located in coincidence ith the $M \geq 4.0$ dividing line separating Zones A and B. The trend depicted by these events might correspond to one of the northeast-southwest steeply dipping faults discussed by *Boyle and Zoback* [2014], and we argue that they might single out the shear zone identified by *Beall and Wright* [2010] separating Zones A and B. These events are characterized by higher values of the source radius for a given magnitude with respect to all the others (Figure 6d). Therefore, we believe that these findings might contribute to the discussion between *Boyle and Zoback* [2014] and *Jeanne et al.* [2014a] concerning the potential of this kind of northeast-southwest steeply dipping faults to favor fluid pressure diffusion or not.

A final topic of discussion concerns the deviation for most of the analyzed events from self-similarity, indicating a different dynamic rupture processes between smaller and larger earthquakes. In our case, we only observe constant $\Delta\sigma$ with the increase of seismic moment for the subset of events showing relatively high η_{SW}. All the other events show a strong increase in stress drop with seismic moment (Figure 7). While a general rule is to observe a trend toward self-similarity for large earthquake populations [e.g., *Allmann and Shearer*, 2009; *Oth et al.*, 2010; *Oth*, 2013], studies on individual earthquake sequences quite often find strong nonself-similar behavior [e.g., *Mayeda et al.*, 2005; *Venkataraman et al.*, 2006]. In this work, we find nonself-similar behavior, γ larger than 2 and small η_{SW}. All these findings suggest that the fault strength at TG is in general not scale-invariant and with the increase of magnitude (i.e., rupture dimension) less high-frequency radiation is generated because required by the rupture process (i.e., required to overcome the friction or for the creation of new fractures surface). *Malagnini et al.* [2010] invoked the mechanisms of dynamic frictional weakening and fault lubrification with increasing fault slip to explain increased stress drop and seismic energy release from larger earthquakes. In the case of TG both these latter processes might play a significant role in controlling the seismicity.

7. Conclusions

We computed accurate seismic source parameters for a large data set of induced earthquakes at TG geothermal field using a novel approach that combines nonparametric, data-driven strategy with an enhanced genetic algorithm. In the first step of the analysis the GIT allows an effective removal from the earthquake recording of the attenuation and site contributions. The retrieved source spectra are therefore inverted for the estimation of source parameters by a nonlinear sensitivity-driven inversion scheme that simultaneously explores the parameters space locally and globally for optimal solutions by using several models.

The main results of our study can be summarized as follows:

1. Most of the seismicity at TG is characterized by low stress drop (i.e., $\Delta\sigma$ between 0.01 and 2.9 MPa and median ~ 0.15 MPa), empirical source spectra that agree with ω^{γ} source model where $\gamma > 2$ (i.e., mostly ~2.5), seismic radiation efficiency indicating positive overshoot, and deviation from self-similarity. Such findings support the idea that smaller and larger earthquakes occur with different dynamic rupture processes. Furthermore, at least for the smaller events, we hypothesize that rock rheology, temperature, and fluid composition contribute to speed up self-healing processes and most of the energy involved in the rupture process is spent for the creation of new fracture surface and by friction.
2. A family of events in the magnitude range M_w 2.5–3.5 confined in the deepest portion of the reservoir is spatially distributed according to the regional fault trend and characterized by relatively high $\Delta\sigma$ values. This family is interpreted to be related to the reactivation of deep structures linked to the regional tectonics, as hypothesized by *Kwiatek et al.* [2015].
3. Finally, we found a further family of events with magnitude mostly in the range M_w 2–2.5 for which the ω^2 source model provides a good description of the source spectral shape and who present relatively high η_{SW} and low $\Delta\sigma$. The peculiar spatial distribution of these events suggests that they occur along a northeast-southwest steeply dipping fault that, as discussed by *Beall and Wright* [2010] and *Boyle and Zoback* [2014], plays an important role in the fluid pressure diffusion.

Acknowledgments
We would like to thank the Editor Y. Ben-Zion and two anonymous reviewers for their comments and suggestions that allowed us to significantly improve the manuscript content and form. This research was carried out in the frame of Programme STAR (project TIMeS), financially supported by UniNA and Compagnia di San Paolo, and partly by the project SHEER (Shale Gas Exploration and Exploitation Induced Risks, financed from the European Union's Horizon 2020 research and innovation program under grant agreement 640896; http://www.sheerproject.eu). Waveform data, metadata, and parametric data of the Lawrence Berkeley National Laboratory Geysers/Calpine seismic network for this study were accessed through the Northern California Earthquake Data Center (NCEDC; network code BG; http://www.ncedc.org, doi:10.7932/NCEDC).

References

Abercrombie, R. E. (1995), Earthquake source scaling relationships from 1 to 5 M_L using seismograms recorded at 2.5 km depth, *J. Geophys. Res.*, *100*, 24,015–24,036, doi:10.1029/95JB02397.

Abercrombie, R. E. (2013), Comparison of direct and coda wave stress drop measurements for the Wells, Nevada, earthquake sequence, *J. Geophys. Res. Solid Earth*, *118*, 1458–1470, doi:10.1029/2012JB009638.

Abercrombie, R. E., and P. C. Leary (1993), Source parameters of small earthquakes recorded at 2.5 km depth, Cajon Pass, southern California: Implications for earthquake scaling, *Geophys. Res. Lett.*, *20*, 1511–1514, doi:10.1029/93GL00367.
Allmann, B. B., and P. M. Shearer (2009), Global variations of stress drop for moderate to large earthquakes, *J. Geophys. Res.*, *114*, B01310, doi:10.1029/2009JB005821.
Ameri, G., A. Oth, M. Pilz, D. Bindi, S. Parolai, L. Luzi, M. Mucciarelli, and G. Cultrera (2011), Separation of source and site effects by generalized inversion technique using the aftershock recordings of the 2009 L'Aquila earthquake, *Bull. Earthquake Eng.*, *9*(3), 717–739.
Amoroso, O., A. Ascione, S. Mazzoli, J. Virieux, and A. Zollo (2014), Seismic imaging of a fluid storage in the actively extending Apennine mountain belt, southern Italy, *Geophys. Res. Lett.*, *41*, 3802–3809, doi:10.1002/2014GL060070.
Amoroso, O., G. De Landro, G. Russo, and A. Zollo (2015), 4D imaging of elastic/anelastic medium properties: Application to the Geysers geothermal area, Conference Paper AGIS Schatzalp Workshop on Induced Seismicity, Davos Schatzalp, Switzerland.
Arai, H., and K. Tokimatsu (2004), S-wave velocity profiling by inversion of microtremor H/V spectrum, *Bull. Seismol. Soc. Am.*, *94*(1), 53–63.
Atkinson, G. M. (2004), Empirical attenuation of ground-motion spectral amplitudes in southeastern Canada and the northeastern United States, *Bull. Seismol. Soc. Am.*, *94*, 1079–1095.
Atkinson, G. M. (2012), Evaluation of attenuation models for the northeastern United States/southeastern Canada, *Seismol. Res. Lett.*, *83*, 166–178.
Beall, J. J., and M. C. Wright (2010), Southern extent of The Geysers high temperature reservoir based on seismic and geochemical evidence, in *GRC Transactions, Geothermal Resources Council*, vol. 34, pp. 1199–1202, Geothermal Resour. Counc., Davis, Calif.
Beall, J. J., M. C. Wright, A. S. Pingol, and P. Atkinson (2010), Effect of high rate injection on seismicity in The Geysers, in *GRC Transactions, Geothermal Resources Council*, vol. 34, pp. 1203–1208, Geothermal Resourc. Counc., Davis, Calif.
Beeler, N. M., T. F. Wong, and S. H. Hickman (2003), On the expected relationships among apparent stress, static stress drop, effective shear fracture energy, and efficiency, *Bull. Seismol. Soc. Am.*, *93*, 1381–1389.
Bertani, R. (2012), Geothermal power generation in the world 2005–2010 update report, *Geothermics*, *41*, 1–29, doi:10.1016/j.geothermics.2011.10.001.
Bindi, D., L. Luzi, S. Parolai, D. Di Giacomo, and G. Monachesi (2011), Site effects observed in alluvial basins: The case of Norcia (Central Italy), *Bull. Earthquake Eng.*, *9*(6), 1941–1959.
Boore, D. M., and J. Boatwrigth (1984), Average body-wave radiation coefficients, *Bull. Seismol. Soc. Am.*, *74*(5), 1615–1621.
Boyle, K., and M. Zoback (2014), The state of stress of the northwest Geysers, California geothermal field, and implications for fault-controlled fluid flow, *Bull. Seismol. Soc. Am.*, *104*, 2303–2312.
Brune, J. N. (1970), Tectonic stress and the spectra of seismic shear waves from earthquakes, *J. Geophys. Res.*, *75*, 4997–5009, doi:10.1029/JB075i026p04997.
Castro, R. R., J. G. Anderson, and S. K. Singh (1990), Site response, attenuation and source spectra of *S* waves along the Guerrero, Mexico, subduction zone, *Bull. Seismol. Soc. Am.*, *80*(6), 1481–1503.
Castro, R. R., F. Pacor, D. Bindi, G. Franceschina, and L. Luzi (2004), Site response of strong motion stations in the Umbria, Central Italy, region, *Bull. Seismol. Soc. Am.*, *94*(2), 576–590.
Castro, R. R., F. Pacor, R. Puglia, G. Ameri, J. Letort, M. Massa, and L. Luzi (2013), The 2012 May 20 and 29, Emilia earthquakes (Northern Italy) and the main aftershocks: S-wave attenuation, acceleration source functions and site effects, *Geophys. J. Int.*, *195*, 597–611.
Chapman, M. C., and R. W. Godbee (2012), Modeling geometrical spreading and the relative amplitudes of vertical and horizontal high frequency ground motions in eastern North America, *Bull. Seismol. Soc. Am.*, *102*, 1957–1975.
Convertito, V., N. Maercklin, N. Sharma, and A. Zollo (2012), From induced seismicity to direct time-dependent seismic hazard, *Bull. Seismol. Soc. Am.*, *102*, 2563–2573, doi:10.1785/0120120036.
Convertito V., Zollo A., Sharma N., Orefice A., and A. Emolo (2015), Earthquake source parameters and scaling relationships at The Geysers geothermal field, California, AGIS Schatzalp Workshop on Induced Seismicity, Davos, Switzerland, from March 10 to 15, 2015, Davos. [Available at http://www.seismo.ethz.ch/research/groups/schatzalp/Download/S4P01_Convertito.pdf.]
Deichmann, N. (2006), Local magnitude, a moment revisited, *Bull. Seismol. Soc. Am.*, *96*, 1267–1277.
Deichmann, N., and D. Giardini (2009), Earthquakes induced by the stimulation of an enhanced geothermal system below Basel (Switzerland), *Seismol. Res. Lett.*, *80*(5), 784–798, doi:10.1785/gssrl.80.5.784.
Eberhart-Phillips, D., and D. H. Oppenheimer (1984), Induced seismicity in The Geysers geothermal area, California, *J. Geophys. Res.*, *89*, 1191–1207, doi:10.1029/JB089iB02p01191.
Efron, B. (1979), Bootstrap methods: Another look at the jackknife, *Ann. Stat.*, *7*(1), 1–26, doi:10.1214/aos/1176344552.
Ellsworth, W. L. (2013), Injection-induced earthquakes, *Science*, *341*(6142), doi:10.1126/science.1225942.
Frankel, A. (1991), Mechanisms of seismic attenuation in the crust: Scattering and anelasticity in New York state, South Africa, and southern California, *J. Geophys. Res.*, *96*(B4), 6269–6289, doi:10.1029/91JB00192.
Garcia, J., C. Hartline, M. Walters, and M. Wright (2016), The northwest Geysers EGS demonstration project, California. Part 1: Characterization and response to injection, *Geothermics*, *63*, 97–119, doi:10.1016/.j.geothermics.2015.08.003.
Giardini, D. (2009), Geothermal quake risks must be faced, *Nature*, *462*, 848–849, doi:10.1038/462848a.
Goertz-Allmann, B. P., A. Goertz, and S. Wiemer (2011), Stress drop variations of induced earthquakes at the Basel geothermal site, *Geophys. Res. Lett.*, *38*, L09308, doi:10.1029/2011GL047498.
Goertz-Allmann, B. P., and S. Wiemer (2012), Geomechanical modeling of induced seismicity source parameters and implications for seismic hazard assessment, *Geophysics*, *78*(1), KS25–KS39, doi:10.1190/GEO2012-0102.1.
Hanks, T. C., and H. Kanamori (1979), A moment magnitude scale, *J. Geophys. Res.*, *84*, 2348–2350, doi:10.1029/JB084iB05p02348.
Hanks, T. C., and W. Thatcher (1972), A graphical representation of seismic source parameters, *J. Geophys. Res.*, *77*(23), 4393–4405, doi:10.1029/JB077i023p04393.
Hartline, C. S., M. A. Walters, and M. C. Wright (2015), Three-dimensional structural model building, induced seismicity analysis, drilling analysis, and reservoir management at The Geysers Geothermal Field, Northern California, *Geotherm. Resour. Counc. Trans.*, *39*, 603–614.
Herrmann, R. B. (2002), Computer programs in seismology, version 3.2, Saint Louis University. Press, W.H., Teukolsky, S.A., Vetterling, W.T., Flannery, B.P. (1992), Numerical Recipes in Fortran, 2nd ed., Cambridge Univ. Press.
Holland, J. H. (1975), *Adaptation in Natural and Artificial Systems*, 232 pp., Univ. of Mich. Press, Ann Arbor.
Izutani, Y., and H. Kanamori (2001), Scale-dependence of seismic energy-to-moment ratio for strike-slip earthquakes in Japan, *Geophys. Res. Lett.*, *28*, 4007–4010, doi:10.1029/2001GL013402.
Jeanne, P., J. Rutqvist, C. Hartline, J. Garcia, P. F. Dobson, and M. Walters (2014a), Reservoir structure and properties from geomechanical modeling and microseismicity analysis associated with an enhanced geothermal system at The Geysers, California, *Geothermics*, *51*, 460–469.

Jeanne, P., J. Rutqvist, P. F. Dobson, M. Walters, C. Hartline, and J. Garcia (2014b), The impacts of mechanical stress transfers caused by hydromechanical and thermal processes on fault stability during hydraulic stimulation in a deep geothermal reservoir, *Int. J. Rock Mech. Min. Sci.*, *72*, 149–163.

Kanamori, H., and L. Rivera (2004), Static and dynamic scaling relations for earthquakes and their implications for rupture speed and stress drop, *Bull. Seismol. Soc. Am.*, *94*, 314–319.

Kawase, H. (2006), Site effects derived from spectral inversion method for K-NET, Kik-net, and JMA strong-motion network with Special reference to soil nonlinearity in high PGA records, *Bull. Earthquake Res. Inst., Univ. Tokyo*, *81*, 309–315.

Keilis-Borok, V. I., and T. B. Yanovskaya (1967), Inverse problems of seismology, *Geophys. J.*, *13*, 223–234.

Kwiatek, G., and Y. Ben-Zion (2016), Theoretical limits on detection and analysis of small earthquakes, *J. Geophys. Res. Solid Earth*, *121*, 5898–5916, doi:10.1002/2016JB012908.

Kwiatek, G., K. Plenkers, and G. Dresen (2011), Source parameters of picoseismicity recorded at Mponeng deep gold mine, South Africa: Implications for scaling relations, *Bull. Seismol. Soc. Am.*, *101*(6), 2592–2608, doi:10.1785/0120110094.

Kwiatek, G., F. Bulut, M. Bohnhoff, and G. Dresen (2014), High-resolution analysis of seismicity induced at Berlín geothermal field, El Salvador, *Geothermics*, *52*, 98–111, doi:10.1016/j.geothermics.2013.09.008.

Kwiatek, G., P. Martínez-Garzón, G. Dresen, M. Bohnhoff, H. Sone, and C. Hartline (2015), Effects of long-term fluid injection on induced seismicity parameters and maximum magnitude in northwestern part of The Geysers geothermal field, *J. Geophys. Res. Solid Earth*, *120*, 7085–7101, doi:10.1002/2015JB012362.

Latorre, D., J. Virieux, T. Monfret, V. Monteiller, T. Vanorio, J.-L. Got, and H. Lyon-Caen (2004), A new seismic tomography of Aigion area (Gulf of Corinth, Greece) from the 1991 data set, *Geophys. J. Int.*, *159*, 1013–1031.

Madariaga, R. (1976), Dynamics of an expanding circular fault, *Bull. Seismol. Soc. Am.*, *66*, 639–666.

Malagnini, L., S. Nielsen, K. Mayeda, and E. Boschi (2010), Energy radiation from intermediate to large magnitude earthquakes: Implications for dynamic fault weakening, *J. Geophys. Res.*, *115*, B06319, doi:10.1029/2009JB006786.

Martínez-Garzón, P., M. Bohnhoff, G. Kwiatek, and G. Dresen (2013), Stress tensor changes related to fluid injection at The Geysers geothermal field, California, *Geophys. Res. Lett.*, *40*, 2596–2691, doi:10.1002/grl.50438.

Martínez-Garzón, P., G. Kwiatek, H. Sone, M. Bohnhoff, G. Dresen, and C. Hartline (2014), Spatiotemporal changes, faulting regimes, and source parameters of induced seismicity: A case study from The Geysers geothermal field, *J. Geophys. Res. Solid Earth*, *119*, 8378–8396, doi:10.1002/2014JB011385.

Majer, E. L., and J. E. Peterson (2007), Impact of injection on seismicity at The Geysers, California geothermal field, *Int. J. Rock Mech. Min. Sci.*, *44*, 1079–1090.

Mayeda, K., R. Gok, W. R. Walter, and A. Hofstetter (2005), Evidence for non-constant energy/moment scaling from coda-derived source spectra, *Geophys. Res. Lett.*, *32*, L10306, doi:10.1029/2005GL022405.

McNamara, D. E., L. Gee, H. M. Benz, and M. Chapman (2014), Frequency-dependent seismic attenuation in the eastern United States as observed from the 2011 Central Virginia earthquake and aftershock sequence, *Bull. Seismol. Soc. Am.*, *104*(1), 55–72, doi:10.1785/0120130045.

Mitchell, B. (2010), Epilogue, *Pure Appl. Geophys.*, *167*, 1581.

Oth, A. (2013), On the characteristics of earthquake stress release variations in Japan, *Earth Planet. Sci. Lett.*, *377-378*, 132–141, doi:10.1016/j.epsl.2013.06.037.

Oth, A., D. Bindi, S. Parolai, and F. Wenzel (2008), S-wave attenuation characteristics beneath the Vrancea region in Romania: New insights from the inversion of ground motion spectra, *Bull. Seismol. Soc. Am.*, *98*(5), 2482–2497, doi:10.1785/0120080106.

Oth, A., S. Parolai, D. Bindi, and F. Wenzel (2009), Source spectra and site response from S waves of intermediate-depth Vrancea, Romania, earthquakes, *Bull. Seismol. Soc. Am.*, *99*(1), 235–254, doi:10.1785/0120080059.

Oth, A., D. Bindi, S. Parolai, and D. Di Giacomo (2010), Earthquake scaling characteristics and the scale-(in)dependence of seismic energy-to-moment ratio: Insights from KiK-net data in Japan, *Geophys. Res. Lett.*, *37*, L19304, doi:10.1029/2010GL044572.

Oth, A., D. Bindi, S. Parolai, and D. D. Giacomo (2011), Spectral analysis of K-NET and KIK-net data in Japan. Part II: On attenuation characteristics, source spectra, and site response of borehole and surface stations, *Bull. Seismol. Soc. Am.*, *101*(2), 667–687.

Pacor, F., D. Spallarossa, A. Oth, L. Luzi, R. Puglia, L. Cantore, A. Mercuri, M. D'Amico, and D. Bindi (2016), Spectral models for ground motion prediction in the L'Aquila region (central Italy): Evidence for stress-drop dependence on magnitude and depth, *Geophys. J. Int.*, *204*(2), 697–718, doi:10.1093/gji/ggv448.

Paige, C. C., and M. A. Saunders (1982), LSQR: An algorithm for sparse linear equations and sparse least squares, *ACM Trans. Math Softw.*, *8*(1), 43–71.

Parolai, S., D. Bindi, M. Baumbach, H. Grosser, C. Milkereit, S. Karakisa, and S. Zünbül (2004), Comparision of different site response estimation techniques using aftershocks of 1999 Izmit earthquake, *Bull. Seismol. Soc. Am.*, *94*(3), 1096–1108, doi:10.1785/0120030086.

Parolai, S., M. Picozzi, S. M. Richwalski, and C. Milkereit (2005), Joint inversion of phase velocity dispersion and H/V ratio curves from seismic noise recordings using a genetic algorithm, considering higher modes, *Geophys. Res. Lett.*, *32*, L01303, doi:10.1029/2004GL021115.

Picozzi, M., and D. Albarello (2007), Combining genetic and linearized algorithms for a two-step joint inversion of Rayleigh wave dispersion and H/V spectral ratio curves, *Geophys. J. Int.*, *169*, 189–200.

Picozzi, M., S. Parolai, and S. M. Richwalski (2005), Joint inversion of H/V ratios and dispersion curves from seismic noise: Estimating the S-wave velocity of bedrock, *Geophys. Res. Lett.*, *32*, L11308, doi:10.1029/2005GL022878.

Ross, Z. E., and Y. Ben-Zion (2016), Towards reliable automated estimates of earthquake source properties from body wave spectra, *J. Geophys. Res. Solid Earth*, *121*, 4390–4407, doi:10.1002/2016JB013003.

Sambridge M., and K. Mosegaard (2002), Monte Carlo methods in geophysical inverse problems, *Rev. Geophys.*, *40*(3), 1009, doi:10.1029/2000RG000089.

Savage, J. C., and M. D. Wood (1971), The relation between apparent stress and stress drop, *Bull. Seismol. Soc. Am.*, *61*, 1381.

Sonley, E., and R. E. Abercrombie (2006), Effects of methods of attenuation correction on source parameter determination, in *Earthquakes Radiated Energy and the Physics of Faulting*, edited by R. Abercrombie et al., pp. 91–97, AGU, Washington, D. C.

Stark, M.A. (1992), Microearthquakes—A tool to track injected water in The Geysers geothermal reservoir, geothermal resource council, monograph on The Geysers geothermal field, *Spec. Rep., 17*, 111–117.

Stark, M. (2003), Seismic evidence for a long-lived enhanced geothermal system (EGS) in the Northern Geysers reservoir, *Geotherm. Resour. Counc. Trans.*, *24*, 24–27.

Shearer, P. M., G. A. Prieto, and E. Hauksson (2006), Comprehensive analysis of earthquake source spectra in southern California, *J. Geophys. Res.*, *111*, B06303, doi:10.1029/2005JB003979.

Tenthorey, E., and S. F. Cox (2006), Cohesive strengthening of fault zones during the interseismic period: An experimental study, *J. Geophys. Res.*, *111*, B09202, doi:10.1029/2005JB004122.

Tsuda, K., K. Koketsu, Y. Hisada, and T. Hayakawa (2010), Inversion analysis of site responses in the Kanto Basin using data from a dense strong motion seismograph array, *Bull. Seismol. Soc. Am.*, *100*(3), 1276–1287, doi:10.1785/0120090153.

Venkataraman, A., G. C. Beroza, S. Ide, K. Imanishi, H. Ito, and Y. Iio (2006), Measurements of spectral similarity for microearthquakes in western Nagano, Japan, *J. Geophys. Res.*, *111*, B03303, doi:10.1029/2005JB003834.

Viegas, G., and L. Hutchings (2011), Characterization of induced seismicity near an injection well at the northwest Geysers geothermal field, California, *Geotherm. Resour. Counc. Trans.*, *35*, 1773–1780.

Viegas, G. M., R. E. Abercrombie, and W.-Y. Kim (2010), The 2002 *M*5 Au Sable Forks, NY, earthquake sequence: Source scaling relationships and energy budget, *J. Geophys. Res.*, *115*, B07310, doi:10.1029/2009JB006799.

Wyss, M. (1979), Observation and interpretation of tectonic strain release mechanisms, PhD thesis, Calif. Inst. of Technol., Pasadena.

Yamanaka, H., and H. Ishida (1996), Application of GENERIC algorithms to an inversion of surface-wave dispersion data, *Bull. Seismol. Soc. Am.*, *86*, 436–444.

Yenier, E., and G. Atkinson (2015), Regionally adjustable generic ground-motion prediction equation based on equivalent point-source simulations: Application to central and eastern North America, *Bull. Seismol. Soc. Am.*, *105*, 1989–2009.

Zoback, M. D. (2012), Managing the seismic risk posed by wastewater disposal, *Earth*, *57*, 38–43.

Zollo, A., A. Orefice, and V. Convertito (2014), Source parameter scaling and radiation efficiency of microearth- quakes along the Irpinia fault zone in southern Apennines, Italy, *J. Geophys. Res. Solid Earth*, *119*, 3256–3275, doi:10.1002/2013JB010116.